SCIENTIFIC REPORTS
natureresearch

OPEN

Scalable lateral heterojunction by chemical doping of 2D TMD thin films

Bhim Chamlagain[1], Sajeevi S. Withanage[1], Ammon C. Johnston[1] & Saiful I. Khondaker[1,2]✉

Scalable heterojunctions based on two-dimensional transitional metal dichalcogenides are of great importance for their applications in the next generation of electronic and optoelectronic devices. However, reliable techniques for the fabrication of such heterojunctions are still at its infancy. Here we demonstrate a simple technique for the scalable fabrication of lateral heterojunctions via selective chemical doping of TMD thin films. We demonstrate that the resistance of large area MoS_2 and $MoSe_2$ thin film, prepared via low pressure chalcogenation of molybdenum film, decreases by up to two orders of magnitude upon doping using benzyl viologen (BV) molecule. X-ray photoelectron spectroscopy (XPS) measurements confirms n-doping of the films by BV molecules. Since thin films of MoS_2 and $MoSe_2$ are typically more resistive than their exfoliated and co-evaporation based CVD counterparts, the decrease in resistance by BV doping represents a significant step in the utilization of these samples in electronic devices. Using selective BV doping, we simultaneously fabricated many lateral heterojunctions in 1 cm^2 MoS_2 and 1 cm^2 $MoSe_2$ films. The electrical transport measurements performed across the heterojunctions exhibit current rectification behavior due to a band offset created between the doped and undoped regions of the material. Almost 84% of the fabricated devices showed rectification behavior demonstrating the scalability of this technique.

Two dimensional (2D) layered materials are considered to be promising candidates for applications in electronics, optoelectronics, catalysis, sensor, and energy storage devices[1–6]. In particular, heterojunctions of 2D van der Waals materials involving graphene and transition metal dichalcogendies (TMDs) semiconductors have created enormous attention due to their potential opportunities of designing novel device structures for the discovery of novel physics as well as for their potential applications in the next generation of electronic and optoelectronic devices[6–17]. However, the majority of the techniques that has been demonstrated for heterojunction fabrications are complex and suffer from low yield making them not suitable for scalable device fabrication. Van der Waals heterojunction was first demonstrated in a graphene—tungsten disulfide (WS_2) system and was fabricated by stacking graphene and mechanically exfoliated flakes of WS_2 via deterministic transfer method[18]. Since then, many different techniques have been demonstrated for heterojunction fabrication including mechanical exfoliation and transfer[7,14,19–24], vertical and lateral heterojunction via direct CVD growth[25–32], and vertical heterojunction in TMD thin films[33–35]. The stacking of 2D layered materials by mechanical exfoliation is a widely used method to create van der Waals heterostructures for laboratory research. In this process the mechanically exfoliated thin layer of one TMD is transferred to another type of TMD by using intermediate polymer to form a heterojunction[14,19,36,37]. This process requires days in preparing one heterojunction device due to the complexity in placement of one material on top of the other, thus cannot be scalable, a critical requirement for semiconductor device manufacturing technologies. Selective doping via oxygen and fluorine based plasma, and radiation have also been used in mechanically exfoliated samples to fabricate lateral heterojunctions[38–40] demonstrating proof of concepts and they are not scalable due to difficulties in achieving good yields of samples from mechanical exfoliation.

Individual layer of co-evaporation based chemical vapor deposition (CVD) grown TMDs along with post growth transfer process have been used for the fabrication of heterojunctions[41]. A few successful examples of vertically stacked TMD heterostructures have been demonstrated, however, these heterojunctions are limited to very small areas lacking a control of their location, size, and coverage hindering their scalability. The direct

[1]Department of Physics, NanoScience Technology Center, University of Central Florida, Orlando, FL 32826, USA. [2]School of Electrical Engineering and Computer Science, University of Central Florida, Orlando, FL 32826, USA. ✉email: saiful@ucf.edu

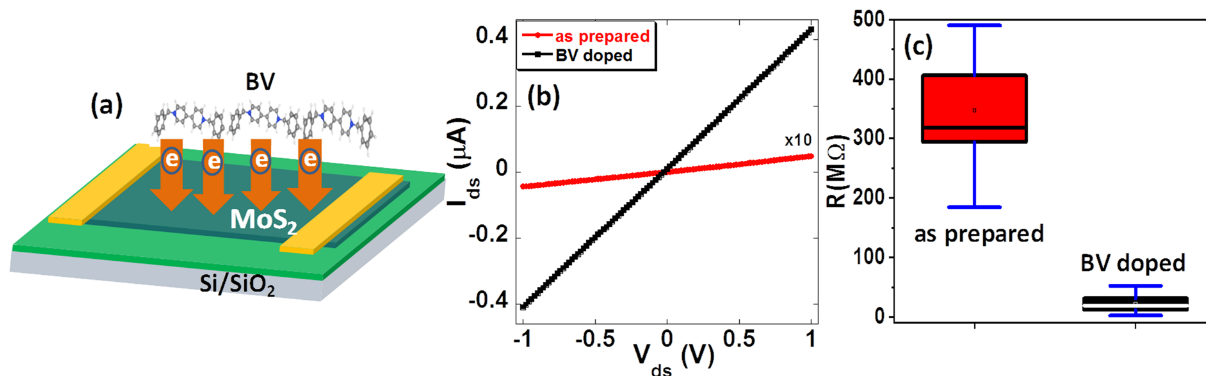

Figure 1. Transport properties of as prepared and BV doped MoS_2 thin film: **(a)** schematic illustration of BV doping of a MoS_2 device, **(b)** I–V characteristics of a representative MoS_2 thin film device before (red) and after BV doping (black). **(c)** Box plot of resistances for 47 MoS_2 thin film devices before and after BV doping.

growth of 2D heterostructure has also been made via chemical vapor deposition (CVD) method[25–32]. The co-evaporation of metal/metal oxides and chalcogen produces many TMDs heterostructures at random locations on the growth substrate[25,28,31,42,43]. However, electrical connections to these heterojunction requires complex fabrication steps. Therefore, the scalability of the co-evaporation based CVD technique for heterojunction device fabrication is uncertain.

While large area TMD thin films, prepared via chalcogenization of metal (molybdenum, tungsten) or metal oxide films[44,45], could be useful in the fabrication of heterojunctions, development of reliable techniques for scalable fabrication is still at its infancy. One useful technique could be the selective chemical doping of 2D TMD thin films for the fabrication of lateral heterojunctions. However, it is not known if the chemical doping can be successfully implemented in TMD thin films. In particular, benzyl viologen (BV) molecules are suggested to be promising candidates for the chemical doping of carbon nanotubes, graphene and other 2D materials[46,47]. BV is a good choice for charge transfer doping, as it has one of the lowest reduction potential among the electron-donating organic molecules[48] and can transfer electrons to a suitable host acceptor material through a direct redox reaction, resulting in a change of carrier concentration in the host material. Therefore, doping of 2D TMD thin films by using BV molecules could change their charge carriers and transport properties and selective doping could open up the possibility of creating a band offset with undoped TMD thin films to fabricate many TMD based heterojunctions in a massively parallel fashion.

In this paper, we demonstrate an effective chemical doping of 2D TMD thin films via BV molecules and use a selective doping technique to fabricate many lateral heterojunctions simultaneously on a single chip. The large area MoS_2 thin films were grown via low pressure sulfurization of Mo films. The electrical characterization performed before and after BV doping show that the resistance of the samples decreased by up to two orders of magnitude upon doping. X-ray photoelectron spectroscopy (XPS) measurements showed a relative shift of peak positions towards higher binding energy values for the BV doped samples suggesting n-doping of the films. The amount of doping can be controlled by sample immersion time to the BV solution. We then implemented a selective area doping method to create doped and undoped-MoS_2 regions to fabricate many lateral heterojunctions simultaneously on a 1 cm^2 chip. The fabricated junctions showed excellent current rectification behavior demonstrating the effectiveness and scalability of this doping method. Similar results for BV doping of $MoSe_2$ thin film along with parallel fabrication of heterojunctions between doped and undoped $MoSe_2$ via selective doping were also demonstrated.

Results and discussion

Large area MoS_2 thin films were prepared via low pressure sulfurization of molybdenum film deposited on a Si/SiO_2 substrate, as described in the method section. Raman characterization confirmed the fabricated samples to be a few layer MoS_2 (supplementary information figure S2). MoS_2 devices of L = 100 μm and W = 300 μm were fabricated by defining drain source electrodes with a shadow mask. Electrical transport measurements of the undoped and BV doped devices were then carried out. The schematic diagram of a MoS_2 device along with charge transfer process from BV molecules to MoS_2 thin film is shown in Fig. 1a. Figure 1b shows a representative low-bias current–voltage ($I_{ds} - V_{ds}$) characteristics of an undoped MoS_2 sample (red curve). The resistance of this sample is calculated to be 215 MΩ. We have used highly doped Si as a back gate, however, no gate dependence was observed consistent with a few other reports[34,49–52]. We have measured 47 MoS_2 devices fabricated on two chips. The resistance of these devices varied from 185 to 490 MΩ with an average of 347 MΩ as shown in the box plot of Fig. 1c. The measured values of resistance for our MoS_2 devices are consistent with what has been reported in the literature[34,49–51,53,54]. After characterizing the as-prepared samples, we doped the MoS_2 film by immersing it in BV solution for 36 h (see "Method" section for detail) and measured their electrical transport properties. Figure 1b black curve shows the I–V characteristics of the same sample represented by the red curve after BV doping. The resistance of the sample changed to 2.4 MΩ, a decrease of ~ 90 times. The significant decrease of resistance (increase of the current) after immersion of the MoS_2 thin film into BV solution indicates that the MoS_2 thin film is strongly doped by the BV molecules due to the transfer of electrons from BV to MoS_2[46,55] via

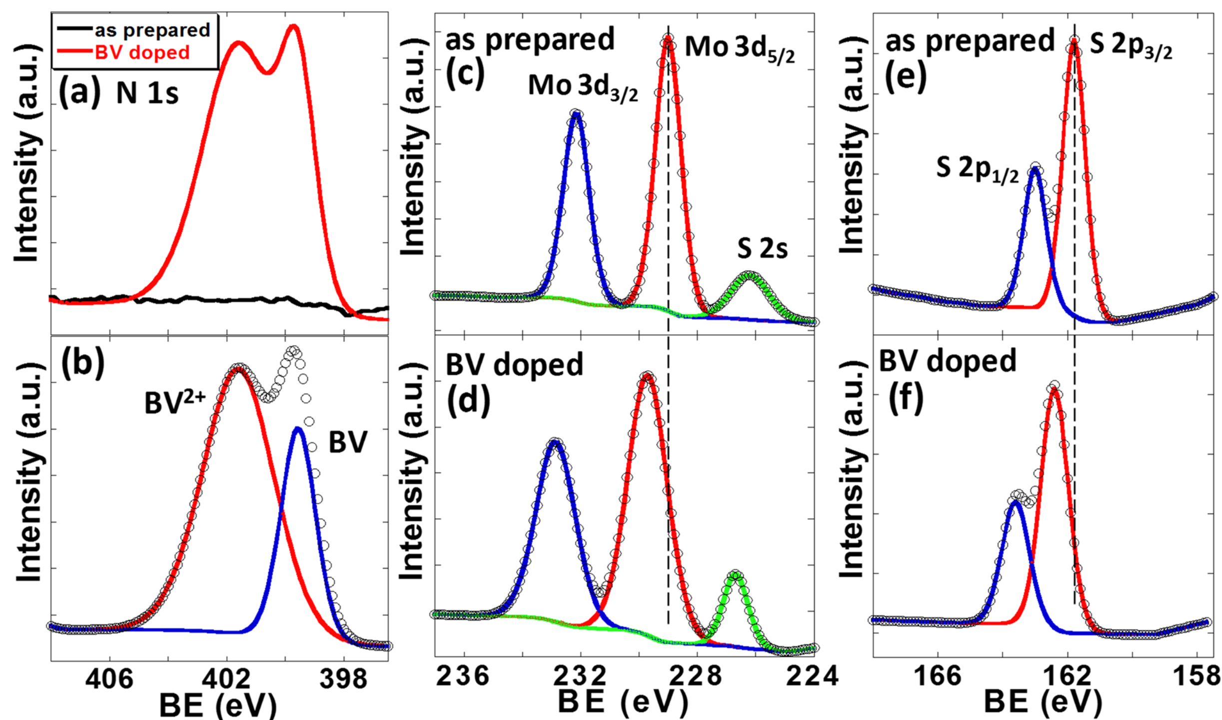

Figure 2. XPS measurements of MoS_2 thin film before and after BV doping: **(a)** N 1s narrow scan of MoS_2 film before and after BV treatment. **(b)** The deconvoluted XPS spectra of N 1s peaks of doped sample (red curve of **(a)**). Mo 3d core level XPS spectra of the **(c)** as prepared and **(d)** BV doped MoS_2 films. The dashed line is a guide to the eye. S 2p XPS spectra of the **(e)** as prepared and **(f)** BV doped MoS_2 films. The spectra were deconvoluted using Gaussian–Lorentzian curves. The symbols are the experimental points and the solid lines are the deconvolution of the data.

surface charge transfer process resulting in an increase of charge carrier concentration. The charge transfer occurs through the redox reaction shown in supplementary Figure S1 (a) and the electron transfer mechanism can be understood by using the schematic diagram shown in supplementary Figure S1 (b). BV is known to have three oxidation states; BV^0 (neutral molecule), BV^+ and BV^{2+} with a reduction potential of – 0.790 V ($BV^+ \rightarrow BV^0$) and -0.332 for ($BV^{2+} \rightarrow BV^+$) vs the standard hydrogen electrode (SHE). On the other hand, MoS_2 is known to have a conduction band edge at around 0 V vs SHE[55]. The lower reduction potential of BV compared to the MoS_2 conduction band edge gives rise to electron transfer from BV to the MoS_2 surface which increases the electronic carrier concentration (decrease of resistance) of MoS_2 channel.

We have measured a total of 47 MoS_2 devices after immersing them in BV solution and found that the resistance for all the samples decreased. This is more clearly shown in the box plot of Fig. 1c. From the box plot, we see that the average resistance of as prepared MoS_2 devices is 347 MΩ, which drops to 22 MΩ after doping. The average resistance of BV doped MoS_2 devices is 94% lower than as prepared MoS_2 devices. Since thin film of MoS_2 is typically more resistive than their exfoliated and co-evaporation based CVD counterparts, the decrease in resistance by BV doping represents a significant step in the utilization of these samples in electronic devices.

To understand the effect of BV doping on MoS_2 thin film, X-ray photoelectron spectroscopy (XPS) measurements were performed for the as prepared and BV doped MoS_2 samples (Fig. 2). BV doped MoS_2 film showed a characteristic N 1s peak that was not seen in untreated MoS_2 film as shown in Fig. 2a. The deconvoluted N 1s narrow scan of BV treated MoS_2 shows peaks at 399.6 eV and 401.9 eV (Fig. 2b). These peaks can be assigned to BV molecule and positively charged BV molecule (BV^{2+})[56,57]. The presence of BV^{2+} peak suggest charge transfer from BV to MoS_2 occurred (also see Figure S1) as the charge transfer will change neutral BV molecule to BV^{2+}. The Mo 3d XPS spectra of as prepared MoS_2 sample showed three prominent peaks at 226.1, 229.0 and 232.1 eV corresponding to binding energies (BEs) of S 2s, Mo $3d_{5/2}$ and Mo $3d_{3/2}$ electrons of MoS_2, respectively (Fig. 2c) which was shifted to 226.8, 229.7 and 232.8 eV, respectively upon BV doping (Fig. 2d). The peaks were shifted towards higher binding energy values by 0.7 eV. S 2p core level XPS spectra of the same sample showed two prominent peaks with peaks position at 161.8 and 163.0 eV corresponding to S $2p_{3/2}$ and S $2p_{1/2}$ spin orbit split components of MoS_2 respectively (Fig. 2e)[52] which was up shifted by 0.65 eV to 162.45 and 163.65 eV, respectively (Fig. 2f). This upshift of BEs of doped MoS_2 film indicates a relative shift of the Fermi level towards the conduction band edge suggesting n-doping of MoS_2 films due to charge transfer by BV molecules, consistent with our electrical transport measurements[58,59]. Raman spectroscopy was also used to characterize BV doped MoS_2 samples (supplementary information Figure S2), however, BV doping only showed a minimal effect on the vibrational modes of the samples.

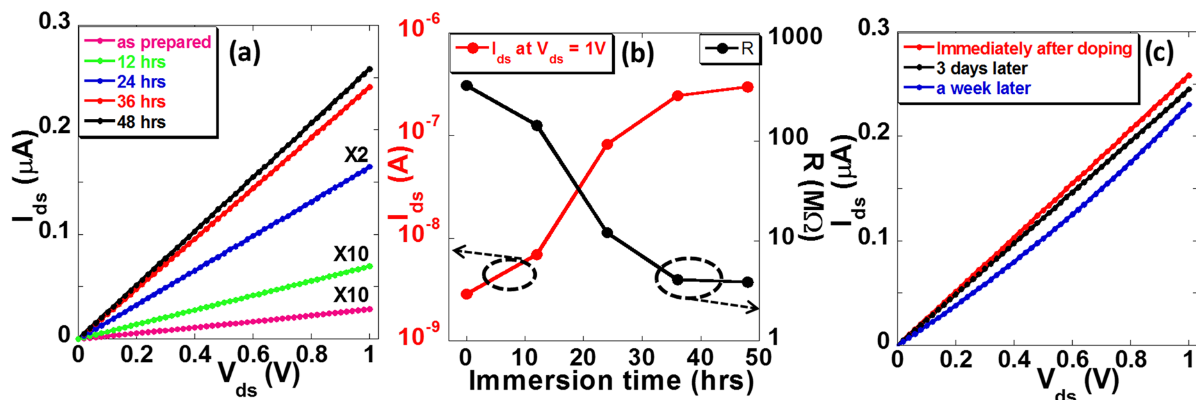

Figure 3. Doping by varying the immersion time and stability of the BV doped MoS_2 thin film: **(a)** I–V characteristics of a BV doped MoS_2 device with different immersion time. **(b)** Current and resistance variation of the MoS_2 device with varying immersion time in BV solution. The current was recorded at $V_{ds} = 1$ V and the resistance was calculated from linear fit of the I–V curve. **(c)** I–V characteristics to show the stability of the doped MoS_2 device. The I–V characteristics were measured immediately after doping, after 3 days and after a week.

We also tested whether the amount of doping can be controlled by varying the immersion time of MoS_2 in the BV solution and measuring the electrical properties of the MoS_2 device after each immersion time. Figure 3a shows I–V characteristics of a representative BV doped MoS_2 device with immersion time varying from 12 to 48 h. The drain current (resistance) increases (decreases) with increasing immersion time and then saturates. We observed the current at $V_{ds} = 1$ V increased from ~ 2.9×10^{-9} A to 7.0×10^{-9} A after 12 h immersion of the MoS_2 device in BV solution resulting in a decrease of resistance from 360 MΩ to 142 MΩ. With further 12 h (total 24 h) soaking of the MoS_2 device in BV solution, the current increased to ~ 8.2×10^{-8} A (resistance decreased to 12.2 MΩ). The current further increased to ~ 2.5×10^{-7} A with an additional 12 h (total 36 h) of immersion resulting in a decrease of resistance to ~ 4.1 MΩ. With further immersion of the MoS_2 device for another 12 h (total of 48 h) in BV solution, resistance decreased to 3.9 MΩ which is a small fraction of change compared to the MoS_2 device with 36 h immersion. The variation of current and resistance with immersion time is more clearly shown in Fig. 3b. It can be seen that the current increases rapidly for the first 24 h and then increases slowly to 36 h. After 36 h, the current almost saturates. When MoS_2 device is immersed in BV solution, BV molecules adsorb on the MoS_2 surface. The BV donates an electron to MoS_2 and changes to another oxidation state (BV^+). The BV^+ further donates an electron to MoS_2 surface and becomes BV^{2+}. More BV molecules adsorb on the MoS_2 surface with increase of immersion time which causes more charges transfer from BV to MoS_2. When the MoS_2 surface is saturated by BV^{2+} molecules, further charge transfer stops. Notably, the BV doped MoS_2 thin film devices are relatively stable with only minimal change in the current over a period of a week (Fig. 3c) The resistance changed from 3.9 MΩ to 4.6 MΩ after a week of ambient exposure.

To test effectiveness of BV doping on other TMD materials, we studied the influence of BV molecules on the transport properties of $MoSe_2$ thin film. The $MoSe_2$ film was prepared via low pressure selenization of Mo film. Raman characterization was carried out to confirm that the synthesized film was a few layer $MoSe_2$ (supplementary information Figure S3). Figure 4a shows I–V curve of a representative undoped $MoSe_2$ device (red curve). The resistance of this sample is calculated to be 388 MΩ. We have measured 27 $MoSe_2$ devices that were fabricated on the same chip and the resistance of the devices varies from 150 MΩ to 410 MΩ with an average of 320 MΩ as shown in the box plot of Fig. 4b. The $MoSe_2$ samples were then immersed in BV solution for 36 h for charge transfer doping process following which the electrical characterizations were carried out. Figure 4a black curve shows the I-V characteristics of the same sample represented by the red curve after BV doping. The resistance of this sample changed to 19 MΩ. We have measured all 27 samples after doping and found that the resistance of all the samples varies from 17 to 55 MΩ with an average of 33 MΩ. This is shown in Fig. 4b. The average resistance decreased by ~ 90% after BV doping of $MoSe_2$ devices. This suggests that, similar to MoS_2 thin film, BV molecules can effectively dope $MoSe_2$ thin film by transferring electrons from BV molecules to $MoSe_2$. XPS measurement of $MoSe_2$ films further confirms the charge transfer based doping. For as prepared $MoSe_2$ thin film, the XPS peaks correspond to Mo $3d_{5/2}$ and $3d_{3/2}$ were observed at binding energies 229.1 and 232.2 eV respectively (Fig. 4c). In addition, the peaks observed at the binding energies of 54.5 and 55.3 eV in the Se 3d spectra can be assigned to the Se $3d_{5/2}$ and Se $3d_{3/2}$ orbitals of $MoSe_2$ (Fig. 4e)[60]. Upon doping the $MoSe_2$ thin film, both Mo 3d and Se 3d peaks were shifted by 0.5 eV to the higher binding energy values (Fig. 4d, f). This upshift of BEs indicates a relative shift of the Fermi level toward the conduction band edge suggesting n-doping of the films[58,59]. This is consistent with MoS_2 XPS measurements.

A selective doping process was developed to fabricate many lateral heterostructure devices simultaneously on a 1 cm^2 chip. Figure 5 shows the schematic diagram of the fabrication steps. First, patterned molybdenum (Mo) film was deposited using a shadow mask (Fig. 5a) followed by the low pressure sulfurization to grow MoS_2 thin film. Cr/Au metal contacts were deposited (Fig. 5b) using another shadow mask. For the selective doping, we coated poly-methyl methacrylate (PMMA) on the MoS_2 thin film and deposited aluminum metal through another shadow mask to cover about half of the MoS_2 channel (Fig. 5c). The regions of the PMMA left uncovered

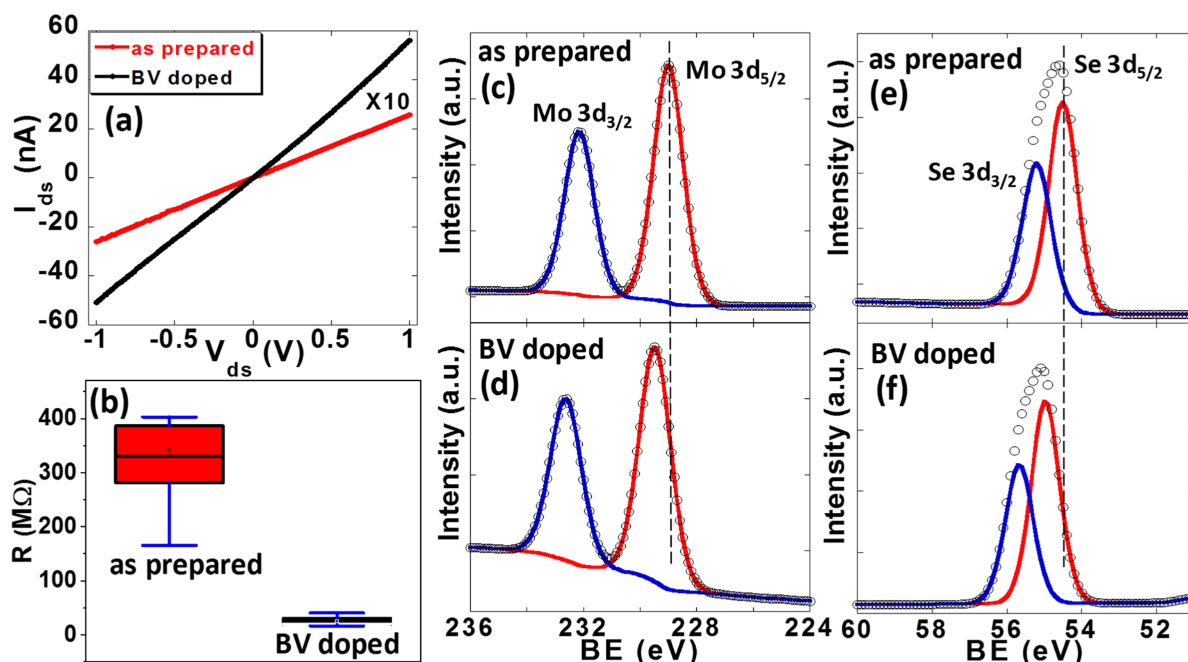

Figure 4. Transport properties and XPS spectra of as prepared and BV doped $MoSe_2$ thin films: **(a)** I–V characteristics of a as-prepared $MoSe_2$ thin film device before (red curve) and after BV doping (black curve). **(b)** Box plot of resistance of 27 $MoSe_2$ devices before and after BV doping. Mo 3d core level XPS spectra of **(c)** a as-prepared and **(d)** BV doped $MoSe_2$ films. The dashed line is a guide to the eye. Se 3d XPS spectra of **(e)** as prepared and **(f)** BV doped $MoSe_2$ films. The spectra were deconvoluted using Gaussian–Lorentzian curves. The symbols are the experimental points and the solid lines are the deconvolution of the data.

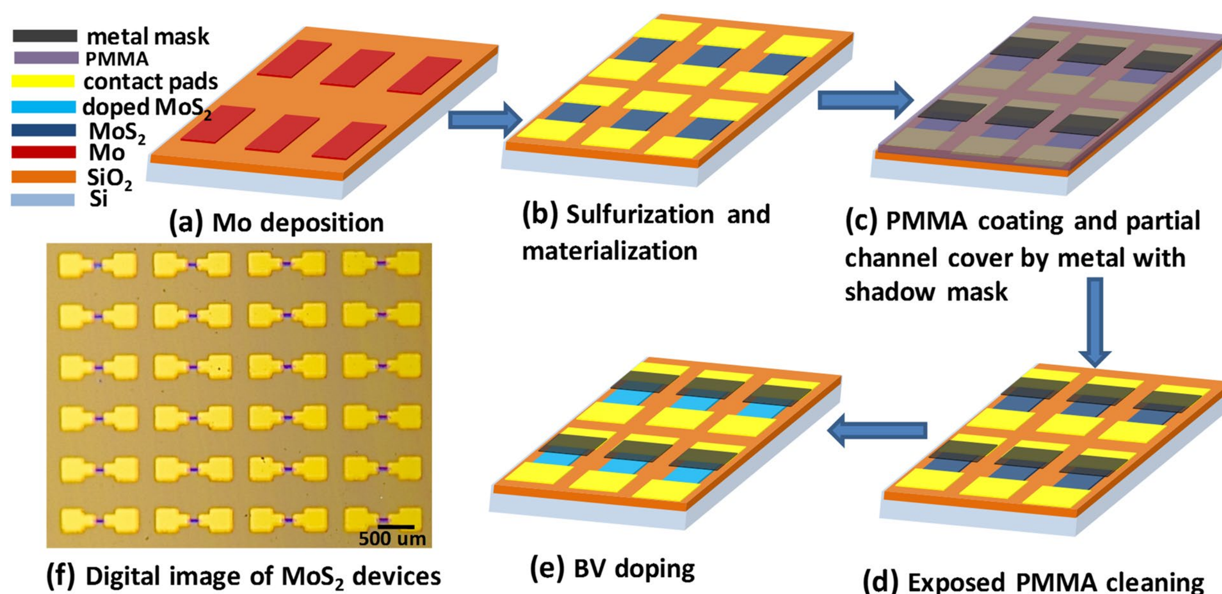

Figure 5. **(a)–(e)** Schematic flow chart showing the different fabrication steps of MoS_2 thin film heterojunctions by selective BV doping technique. Lateral heterojunctions were formed at the junctions of undoped MoS_2 and doped MoS_2 regions. **(f)** Digital image (partial) of MoS_2 heterojunction devices.

with aluminum was etched away using oxygen plasma to partially expose the channel of MoS_2 thin film devices for BV doping (Fig. 5d). The entire substrate was then immersed into BV solution for 36 h. The regions covered by aluminum/PMMA are protected and left unexposed to BV molecules. Only the exposed regions of the MoS_2 channel were doped by BV solution due to charge transfer process. This process creates doped and undoped sides of the MoS_2 channel (Fig. 5e). As a result, heterojunctions are created at the junctions of doped and undoped MoS_2 regions. Since many samples can be simultaneously patterned in the same batch, this process is promising for creating scalable lateral heterojunctions. A digital image showing many heterojunctions created in the

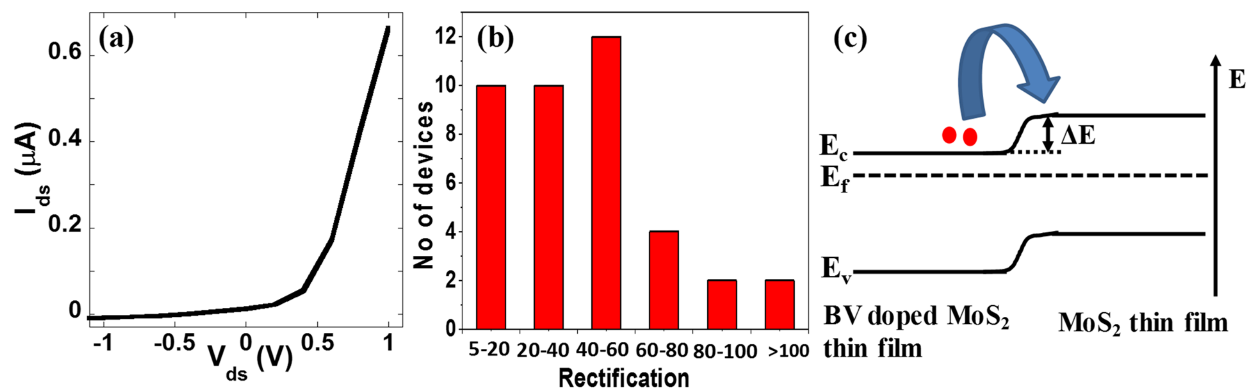

Figure 6. Current rectification characteristics of MoS_2 heterojunction after selective chemical doping: **(a)** I–V characteristics of a MoS_2 heterojunction device prepared by selective BV doping. **(b)** Statistics of rectification behavior of 40 MoS_2 heterojunction devices simultaneously fabricated in a single chip. **(c)** Schematic band diagram showing band offset (ΔE) between the undoped and doped MoS_2 regions.

same chip is presented in Fig. 5f. A high magnification optical image of a single MoS_2 heterojunction device is shown in supplementary information Figure S4. The heterojunction properties were confirmed by the electrical transport measurements.

Figure 6a shows I–V characteristics of a representative selectively doped MoS_2 lateral heterojunction device measured at room temperature. The I–V curve shows nonlinear diode like characteristics, with a very high current for forward bias and negligible current for reverse bias, expected for a heterojunction device. This device did not show reverse bias breakdown for up to − 1.0 V. The rectification ratio ($I_{forward}/I_{reverse}$) of this device is calculated to be ~ 78. As the individual MoS_2 devices did not show any gate dependence, the heterojunction devices did not show any gate dependence characteristics either when highly doped Si was used as back gate. In order to ensure that the measured electrical properties are originated from the fabricated heterojunctions, we monitored the effect of the fabrication process by measuring I–V curves after every fabrication step (supplementary information figure S5). Current rectification behavior was not observed before immersing the samples into the BV solution. In addition, the I–V curves of as fabricated and doped devices are linear (Fig. 1b), suggesting that the observed current rectification behavior is not coming from Schottky contacts between MoS_2/metal electrodes. This observation confirms the formation of the lateral heterojunctions of MoS_2 by selective doping method. We have fabricated a total of 48 MoS_2 lateral junction devices simultaneously on the same 1 cm^2 chip and measured their electrical transport properties. Out of them, 40 devices showed current rectification behavior. Figure 6b summarizes the rectification behavior of all the devices. The lateral junction devices exhibited current rectification behavior with a rectification ratio of up to two orders of magnitude. Notably, the fabricated heterojunction devices are relatively stable and showed minimal change in I–V curve and rectification ratio over a period of a week (supplementary information figure S6) consistent with the observed air stability of BV doped MoS_2 thin film device presented in Fig. 3c. Our result can be explained by the energy-band diagram of Fig. 6c that illustrates the band profiles and band alignment between the undoped MoS_2 and BV doped MoS_2 regions. The work function of the pristine MoS_2 has been reported to be in the range of 4.6–4.9 eV[61–64]. Although, the exact work function of BV doped MoS_2 is not known, we expect this to be lower than MoS_2 due to the increased carrier concentration by doping as the work function is known to be modulated by p or n-doping[5,65]. This is further supported by the XPS measurements where the characteristics peaks were shifted towards higher binding energy values (Fig. 2) indicating n-doping of the thin film by BV molecules. The n-doping causes a relative shift of fermi level towards the conduction band of MoS_2 resulting in a decrease of work function of the doped part of the channel. This would create a band offset (ΔE) between the doped and undoped regions of MoS_2 resulting in the formation of lateral heterojunctions. This band offset prevents the flow of charge carriers at the negative bias voltages and leads to a rectification behavior. Similar selective doping method has been implemented to simultaneously fabricate many $MoSe_2$ heterojunction devices on a 1 cm^2 chip which also showed excellent current rectification behavior, demonstrating the scalability of the technique (supplementary information figure S7).

Conclusion

We demonstrated a simple technique for the doping of TMD thin films and used selective doping for scalable fabrication of lateral heterojunctions. We show for the first time that when MoS_2 and $MoSe_2$ thin films, grown via low pressure sulfurization and selenization of Mo films, are immersed into BV solution, the resistance decreases by up to two-orders of magnitude due to the surface charge transfer based doping. XPS measurements show a relative shift of characteristics peak positions towards higher BEs for the doped samples indicating an n-doping of the films by BV molecules. The amount of doping can be controlled by varying the immersion time of the thin film devices in BV solution. Using a simple patterning technique, we implemented selective doping of MoS_2 samples and fabricated many MoS_2 lateral heterojunction devices simultaneously on a 1 cm^2 chip. The electrical transport measurements performed across MoS_2 junction exhibit current rectification behavior with a rectification ration of up to two orders of magnitude due to the band offset created by selective doping. Similar heterojunction devices via selective doping was also demonstrated in $MoSe_2$ thin film which exhibits current rectification behavior.

The doping method presented here provides an efficient way to control the electrical properties of TMDs based thin film and when combined with the selective doping technique to fabricate scalable heterostructure devices.

Methods

MoS_2 and $MoSe_2$ film growth. Molybdenum (Mo) film of 6 nm thickness was deposited by an electron beam evaporator at a low evaporation rate of 0.05 Å/s on a Si/SiO_2 substrates with 250 nm of thermal oxide layer. The substrate was then placed in the center zone of one-inch quartz tube furnace (Barnstead International F79300 Tube Furnace) and an alumina boat containing sulfur (S) powder was placed in the furnace upstream side. The system was pumped down to a base pressure of ~30 mTorr and purged argon (Ar) gas to remove oxygen and water vapor. The Ar gas flow of ~130 standard cubic centimeters per minute (sccm) was maintained during entire growth process. The furnace was heated to the growth temperature of 800 °C with ramping rate of 15°/min and was maintained at the growth temperature for 55 min. The sulfur vapor was carried by Ar gas to the central zone where it reacts with the Mo to form MoS_2 films. The chamber was allowed to cool down to room temperature naturally after growth. $MoSe_2$ film was prepared by selenization of the 2 nm Mo metal film using same method as MoS_2 film preparation.

Raman characterization. Raman characterization was performed using a Witec alpha 300 RA confocal Raman microscope with laser source of excitation wavelength of 532 nm and power of < 1 mW in ambient conditions at room temperature. A 100 × objective was used to focus the laser beam at a spot. Raman emission was collected and dispersed by a grating of 1,800 lines-per-mm with the data accumulation duration of 3 s.

XPS characterization. XPS measurements of the TMD films were performed using a Thermo Scientific (Escalab Xi) XPS system with a monochromatic Al Kα radiation source. Pass energy of 20 eV with 0.1 eV scanning step was used for photoelectron detection. XPS spectra were taken onto the sample surface with a scan area 300 × 300 μm^2 and carbon (C) 1 s reference line at the binding energy of 284.8 eV was used to calibrate the charging effect.

Device fabrication and transport characterization. For the electrical transport characterization of as prepared and BV doped MoS_2 and $MoSe_2$ films, 5 nm/40 nm Cr/Au electrodes were patterned on top of MoS_2 and $MoSe_2$ films using a shadow mask. The electrodes were deposited with a deposition rate of 0.05 Å/s at a base pressure of 5×10^{-7} mBar. The electrical transport measurements of the devices were performed in a probe station using a current preamplifier (DL instruments 1211) interfaced with Lab View program. All electrical measurements were carried out at room temperature in ambient conditions.

Synthesis of benzyl viologen (BV) and doping. 25 mg benzyl viologen dichloride (Sigma-Aldrich) was dissolved into 5 ml of nanopure DI water. 5 ml of toluene was added to benzyl viologen dichloride and water to make a bilayer solution. ~ 3.7 gm of Sodium borohydride (Sigma-Aldrich) was added to the water/toluene bilayer solution. The solution was then kept for one day to form benzyl viologen (BV). The BV accumulated in the toluene solution. The toluene solution with BV molecules was carefully extracted using pipette. The MoS_2 and $MoSe_2$ devices was immersed into the extracted BV solution for doping of the thin films. The doping was performed by immersion of the MoS_2 and $MoSe_2$ devices into the BV solution for 12 to 48 h. The samples were then taken out of the solution and allowed to dry naturally.

Data availability

The data that support the findings of this study are available from the corresponding author upon reasonable request.

Received: 7 April 2020; Accepted: 20 July 2020
Published online: 31 July 2020

References

1. Alarawi, A., Ramalingam, V. & He, J.-H. Recent advances in emerging single atom confined two-dimensional materials for water splitting applications. *Mater. Today Energy* **11**, 1–23. https://doi.org/10.1016/j.mtener.2018.10.014 (2019).
2. Sriram, P., Manikandan, A., Chuang, F. C. & Chueh, Y. L. Hybridizing plasmonic materials with 2D-transition metal dichalcogenides toward functional applications. *Small* **16**, e1904271. https://doi.org/10.1002/smll.201904271 (2020).
3. Manikandan, A. *et al.* A superior dye adsorbent towards the hydrogen evolution reaction combining active sites and phase-engineering of (1T/2H) MoS2/α-MoO3 hybrid heterostructured nanoflowers. *J. Mater. Chem. A* **6**, 15320–15329. https://doi.org/10.1039/c8ta02496k (2018).
4. Fu, H. C. et al. MXene-contacted silicon solar cells with 11.5% efficiency. *Adv. Energy Mater.* 9, 1900180, https://doi.org/10.1002/aenm.201900180 (2019).
5. Yun, J.-M. *et al.* Efficient work-function engineering of solution-processed MoS_2 thin-films for novel hole and electron transport layers leading to high-performance polymer solar cells. *J. Mater. Chem. C* **1**, 3777. https://doi.org/10.1039/c3tc30504j (2013).
6. Wang, Q. H., Kalantar-Zadeh, K., Kis, A., Coleman, J. N. & Strano, M. S. Electronics and optoelectronics of two-dimensional transition metal dichalcogenides. *Nat. Nanotechnol.* **7**, 699–712. https://doi.org/10.1038/nnano.2012.193 (2012).
7. Choi, M. S. *et al.* Controlled charge trapping by molybdenum disulphide and graphene in ultrathin heterostructured memory devices. *Nat. Commun.* **4**, 1624. https://doi.org/10.1038/ncomms2652 (2013).
8. Roy, K. *et al.* Graphene-MoS_2 hybrid structures for multifunctional photoresponsive memory devices. *Nat. Nanotechnol.* **8**, 826–830. https://doi.org/10.1038/nnano.2013.206 (2013).
9. Lin, Y. C. *et al.* Atomically thin resonant tunnel diodes built from synthetic van der Waals heterostructures. *Nat. Commun.* **6**, 7311. https://doi.org/10.1038/ncomms8311 (2015).

10. Yu, W. et al. Near-infrared photodetectors based on $MoTe_2$/graphene heterostructure with high responsivity and flexibility. *Small* 13, https://doi.org/10.1002/smll.201700268 (2017).
11. Myoung, N., Seo, K., Lee, S. J. & Ihm, G. Large current modulation and spin-dependent tunneling of vertical graphene/MoS_2 heterostructures. *ACS Nano* **7**, 7021–7027. https://doi.org/10.1021/nn402919d (2013).
12. Safeer, C. K. *et al.* Room-temperature spin Hall effect in graphene/MoS_2 van der Waals heterostructures. *Nano Lett.* **19**, 1074–1082. https://doi.org/10.1021/acs.nanolett.8b04368 (2019).
13. Das, S., Gulotty, R., Sumant, A. V. & Roelofs, A. All two-dimensional, flexible, transparent, and thinnest thin film transistor. *Nano Lett.* **14**, 2861–2866. https://doi.org/10.1021/nl5009037 (2014).
14. Lee, C. H. *et al.* Atomically thin p-n junctions with van der Waals heterointerfaces. *Nat. Nanotechnol.* **9**, 676–681. https://doi.org/10.1038/nnano.2014.150 (2014).
15. Chhowalla, M. *et al.* The chemistry of two-dimensional layered transition metal dichalcogenide nanosheets. *Nat. Chem.* **5**, 263–275. https://doi.org/10.1038/nchem.1589 (2013).
16. Wang, B. *et al.* Bifunctional NbS_2-based asymmetric heterostructure for lateral and vertical electronic devices. *ACS Nano* **14**, 175–184. https://doi.org/10.1021/acsnano.9b06627 (2020).
17. Alarawi, A. *et al.* Enhanced photoelectrochemical hydrogen production efficiency of MoS_2-Si heterojunction. *Opt. Express* **27**, A352–A363. https://doi.org/10.1364/OE.27.00A352 (2019).
18. Georgiou, T. *et al.* Vertical field-effect transistor based on graphene-WS_2 heterostructures for flexible and transparent electronics. *Nat. Nanotechnol.* **8**, 100–103. https://doi.org/10.1038/nnano.2012.224 (2013).
19. Chiu, M. H. *et al.* Determination of band alignment in the single-layer MoS_2/WSe_2 heterojunction. *Nat. Commun.* **6**, 7666. https://doi.org/10.1038/ncomms8666 (2015).
20. Hong, T. *et al.* Anisotropic photocurrent response at black phosphorus-MoS_2 p-n heterojunctions. *Nanoscale* **7**, 18537–18541. https://doi.org/10.1039/c5nr03400k (2015).
21. Ju, L. *et al.* Photoinduced doping in heterostructures of graphene and boron nitride. *Nat. Nanotechnol.* **9**, 348–352. https://doi.org/10.1038/nnano.2014.60 (2014).
22. Fang, H. et al. Strong interlayer coupling in van der Waals heterostructures built from single-layer chalcogenides. *Proc. Natl. Acad. Sci. USA* **111**, 6198–6202, https://doi.org/10.1073/pnas.1405435111 (2014).
23. Furchi, M. M., Pospischil, A., Libisch, F., Burgdorfer, J. & Mueller, T. Photovoltaic effect in an electrically tunable van der Waals heterojunction. *Nano Lett.* **14**, 4785–4791. https://doi.org/10.1021/nl501962c (2014).
24. Duong, N. T. *et al.* Modulating the functions of MoS_2/$MoTe_2$ van der Waals heterostructure via thickness variation. *ACS Nano* **13**, 4478–4485. https://doi.org/10.1021/acsnano.9b00014 (2019).
25. Bogaert, K. *et al.* Diffusion-mediated synthesis of MoS_2/WS_2 lateral heterostructures. *Nano Lett.* **16**, 5129–5134. https://doi.org/10.1021/acs.nanolett.6b02057 (2016).
26. Sahoo, P. K., Memaran, S., Xin, Y., Balicas, L. & Gutierrez, H. R. One-pot growth of two-dimensional lateral heterostructures via sequential edge-epitaxy. *Nature* **553**, 63–67. https://doi.org/10.1038/nature25155 (2018).
27. Duan, X. *et al.* Lateral epitaxial growth of two-dimensional layered semiconductor heterojunctions. *Nat. Nanotechnol.* **9**, 1024–1030. https://doi.org/10.1038/nnano.2014.222 (2014).
28. Gong, Y. *et al.* Two-step growth of two-dimensional WSe_2/$MoSe_2$ heterostructures. *Nano Lett.* **15**, 6135–6141. https://doi.org/10.1021/acs.nanolett.5b02423 (2015).
29. Li, M. Y. *et al.* Nanoelectronics. Epitaxial growth of a monolayer WSe_2-MoS_2 lateral p-n junction with an atomically sharp interface. *Science* 349, 524–528, https://doi.org/10.1126/science.aab4097 (2015).
30. Kang, K. *et al.* Layer-by-layer assembly of two-dimensional materials into wafer-scale heterostructures. *Nature* **550**, 229–233. https://doi.org/10.1038/nature23905 (2017).
31. Zhang, Z. *et al.* Robust epitaxial growth of two-dimensional heterostructures, multiheterostructures, and superlattices. *Science* **357**, 788–792. https://doi.org/10.1126/science.aan6814 (2017).
32. Mandyam, S. V. *et al.* Controlled growth of large-area bilayer tungsten diselenides with lateral p-n Junctions. *ACS Nano* **13**, 10490–10498. https://doi.org/10.1021/acsnano.9b04453 (2019).
33. Xue, Y. *et al.* Scalable production of a few-layer MoS_2/WS_2 vertical heterojunction array and its application for photodetectors. *ACS Nano* **10**, 573–580. https://doi.org/10.1021/acsnano.5b05596 (2016).
34. Choudhary, N. *et al.* Centimeter scale patterned growth of vertically stacked few layer only 2D MoS_2/WS_2 van der Waals heterostructure. *Sci. Rep.* **6**, 25456. https://doi.org/10.1038/srep25456 (2016).
35. Islam, M. A. *et al.* Centimeter-scale 2D van der Waals vertical heterostructures integrated on deformable substrates enabled by gold sacrificial layer-assisted growth. *Nano Lett.* **17**, 6157–6165. https://doi.org/10.1021/acs.nanolett.7b02776 (2017).
36. Zhou, R., Ostwal, V. & Appenzeller, J. Vertical versus lateral two-dimensional heterostructures: on the topic of atomically abrupt p-n junctions. *Nano Lett.* **17**, 4787–4792. https://doi.org/10.1021/acs.nanolett.7b01547 (2017).
37. Yan, X. *et al.* Tunable $SnSe_2$/WSe_2 heterostructure tunneling field effect transistor. *Small* **13**, 1701478. https://doi.org/10.1002/smll.201701478 (2017).
38. Choudhary, N. *et al.* Two-dimensional lateral heterojunction through bandgap engineering of MoS_2 via oxygen plasma. *J. Phys. Condens. Matter.* **28**, 364002. https://doi.org/10.1088/0953-8984/28/36/364002 (2016).
39. Chen, M. *et al.* Stable few-layer MoS_2 rectifying diodes formed by plasma-assisted doping. *Appl. Phys. Lett.* **103**, 142110. https://doi.org/10.1063/1.4824205 (2013).
40. Stanford, M. G. *et al.* Focused helium-ion beam irradiation effects on electrical transport properties of few-layer WSe_2: Enabling nanoscale direct write homo-junctions. *Sci. Rep.* **6**, 27276. https://doi.org/10.1038/srep27276 (2016).
41. Hong, X. *et al.* Ultrafast charge transfer in atomically thin MoS_2/WS_2 heterostructures. *Nat. Nanotechnol.* **9**, 682–686. https://doi.org/10.1038/nnano.2014.167 (2014).
42. Gong, Y. *et al.* Vertical and in-plane heterostructures from WS_2/MoS_2 monolayers. *Nat. Mater.* **13**, 1135–1142. https://doi.org/10.1038/nmat4091 (2014).
43. Wang, L., Tahir, M., Chen, H. & Sambur, J. B. Probing charge carrier transport and recombination pathways in monolayer MoS_2/WS_2 heterojunction photoelectrodes. *Nano Lett.* **19**, 9084–9094. https://doi.org/10.1021/acs.nanolett.9b04209 (2019).
44. Kong, D. *et al.* Synthesis of MoS_2 and $MoSe_2$ films with vertically aligned layers. *Nano Lett.* **13**, 1341–1347. https://doi.org/10.1021/nl400258t (2013).
45. Simchi, H. *et al.* Sulfidation of 2D transition metals (Mo, W, Re, Nb, Ta): thermodynamics, processing, and characterization. *J. Mater. Sci.* **52**, 10127–10139. https://doi.org/10.1007/s10853-017-1228-x (2017).
46. Kim, S. M. *et al.* Reduction-controlled viologen in bisolvent as an environmentally stable n-type dopant for carbon nanotubes. *J. Am. Chem. Soc.* **131**, 327–331. https://doi.org/10.1021/ja807480g (2009).
47. Yu, W. J., Liao, L., Chae, S. H., Lee, Y. H. & Duan, X. Toward tunable band gap and tunable dirac point in bilayer graphene with molecular doping. *Nano Lett.* **11**, 4759–4763. https://doi.org/10.1021/nl2025739 (2011).
48. Suzuki, M., Morris, N. D. & Mallouk, T. E. Photosensitized production of doubly reduced methylviologen followed by highly efficient methylviologen radical formation using self-assembling ruthenium(II) complexes. *Chem. Commun.* 1534–1535, https://doi.org/10.1039/B205076P (2002).
49. Momose, T., Nakamura, A., Daniel, M. & Shimomura, M. Phosphorous doped p-type MoS_2 polycrystalline thin films via direct sulfurization of Mo film. *AIP Adv.* **8**, 025009. https://doi.org/10.1063/1.5019223 (2018).

50. Jung, Y. *et al.* Metal seed layer thickness-induced transition from vertical to horizontal growth of MoS_2 and WS_2. *Nano Lett.* **14**, 6842–6849. https://doi.org/10.1021/nl502570f (2014).
51. Jarvinen, T. *et al.* WS_2 and MoS_2 thin film gas sensors with high response to NH_3 in air at low temperature. *Nanotechnology* **30**, 405501. https://doi.org/10.1088/1361-6528/ab2d48 (2019).
52. Chamlagain, B. & Khondaker, S. I. Electrical properties tunability of large area MoS_2 thin films by oxygen plasma treatment. *Appl. Phys. Lett.* **116**, 223102. https://doi.org/10.1063/5.0008850 (2020).
53. Islam, M. A. *et al.* Noble metal-coated MoS_2 nanofilms with vertically-aligned 2D layers for visible light-driven photocatalytic degradation of emerging water contaminants. *Sci. Rep.* **7**, 14944. https://doi.org/10.1038/s41598-017-14816-9 (2017).
54. Sirota, B., Glavin, N. & Voevodin, A. A. Room temperature magnetron sputtering and laser annealing of ultrathin MoS_2 for flexible transistors. *Vacuum* **160**, 133–138. https://doi.org/10.1016/j.vacuum.2018.10.077 (2019).
55. Kiriya, D., Tosun, M., Zhao, P., Kang, J. S. & Javey, A. Air-stable surface charge transfer doping of MoS_2 by benzyl viologen. *J. Am. Chem. Soc.* **136**, 7853–7856. https://doi.org/10.1021/ja5033327 (2014).
56. Cao, L., Fang, G. & Wang, Y. Electroreduction of viologen phenyl diazonium salts as a strategy to control viologen coverage on electrodes. *Langmuir* **33**, 980–987. https://doi.org/10.1021/acs.langmuir.6b04317 (2017).
57. Alvaro, M., Garcia, H., Garcia, S., Marquez, F. & Scaiano, J. C. Intrazeolite photochemistry. 17. Zeolites as electron donors: Photolysis of methylviologen incorporated within zeolites. *J. Phys. Chem. B* **101**, 3043–3051, https://doi.org/10.1021/jp9628850 (1997)
58. Fan, S. *et al.* Ambipolar and n/p-type conduction enhancement of two-dimensional materials by surface charge transfer doping. *Nanoscale* **11**, 15359–15366. https://doi.org/10.1039/c9nr05343c (2019).
59. Kim, K. H. *et al.* Effect of large work function modulation of MoS_2 by controllable chlorine doping using a remote plasma. *J. Mater. Chem. C* **8**, 1846–1851. https://doi.org/10.1039/c9tc05548g (2020).
60. Truong, Q. D. *et al.* Exfoliated MoS_2 and $MoSe_2$ nanosheets by a supercritical fluid process for a hybrid Mg-Li-ion battery. *ACS Omega* **2**, 2360–2367. https://doi.org/10.1021/acsomega.7b00379 (2017).
61. Dhakal, K. P. *et al.* Probing multiphased transition in bulk MoS_2 by direct electron injection. *ACS Nano* **13**, 14437–14446. https://doi.org/10.1021/acsnano.9b08037 (2019).
62. Kim, J. H. *et al.* Work function variation of MoS_2 atomic layers grown with chemical vapor deposition: The effects of thickness and the adsorption of water/oxygen molecules. *Appl. Phys. Lett.* **106**, 251606. https://doi.org/10.1063/1.4923202 (2015).
63. Lee, S. Y. *et al.* Large work function modulation of monolayer MoS_2 by ambient gases. *ACS Nano* **10**, 6100–6107. https://doi.org/10.1021/acsnano.6b01742 (2016).
64. Lin, J. *et al.* Modulating electronic transport properties of MoS_2 field effect transistor by surface overlayers. *Appl. Phys. Lett.* **103**, 063109. https://doi.org/10.1063/1.4818463 (2013).
65. Choi, M. S. *et al.* Lateral MoS_2 p–n junction formed by chemical doping for use in high-performance optoelectronics. *ACS Nano* **8**, 9332–9340, https://doi.org/10.1021/nn503284n (2014)

Acknowledgements

This work was supported by U.S. National Science Foundation (NSF) under Grants No. 1728309. We also acknowledge Prof. Tetard for Raman spectroscopy measurements support.

Author contributions

B.C. conceived the idea and led the project under the guidance of S.I.K. B.C., A.C.J. and S.S.W. synthesized materials. B.C. synthesized the BV solution, fabricated devices and conducted the electrical and XPS measurements. S.S.W. performed the Raman characterizations. B.C. drafted the manuscript and S.S.W., A.C.J. and S.I.K. participated to complete the manuscript.

Competing interests

The authors declare no competing interests.

Additional information

Supplementary information is available for this paper at https://doi.org/10.1038/s41598-020-70127-6.

Correspondence and requests for materials should be addressed to S.I.K.

Reprints and permissions information is available at www.nature.com/reprints.

Publisher's note Springer Nature remains neutral with regard to jurisdictional claims in published maps and institutional affiliations.

Open Access This article is licensed under a Creative Commons Attribution 4.0 International License, which permits use, sharing, adaptation, distribution and reproduction in any medium or format, as long as you give appropriate credit to the original author(s) and the source, provide a link to the Creative Commons license, and indicate if changes were made. The images or other third party material in this article are included in the article's Creative Commons license, unless indicated otherwise in a credit line to the material. If material is not included in the article's Creative Commons license and your intended use is not permitted by statutory regulation or exceeds the permitted use, you will need to obtain permission directly from the copyright holder. To view a copy of this license, visit http://creativecommons.org/licenses/by/4.0/.

© The Author(s) 2020